




## Conventional high-temperature superconductivity in $\sigma$ -band driven metallized two-dimensional metal borocarbides

Yiming Zhang, Jingyan Chen, Jian Hao, Meiling Xu <sup>\*</sup>, and Yinwei Li <sup>†</sup>  
*Laboratory of Quantum Functional Materials Design and Application, School of Physics  
 and Electronic Engineering, Jiangsu Normal University, Xuzhou 221116, China*

 (Received 19 March 2024; revised 10 August 2024; accepted 13 August 2024; published 23 August 2024)

The superconductivity driven by the strong coupling of  $\sigma$ -bonding electrons with interlayer covalent bond-stretching modes presents a promising pathway for achieving high- $T_c$  superconductivity under atmospheric conditions. Herein, we conduct high-throughput first-principles calculations to comprehensively investigate potential superconductivity in two-dimensional (2D) metal borocarbides ( $MB_2C_2$ ,  $M = \text{metal}$ ). Our analysis of 41  $MB_2C_2$  films reveals that 23 demonstrate dynamical stability and 17 of them are potential superconductors. Moreover, we identify six promising candidates within this subset with critical temperatures  $T_c \geq 75$  K, i.e.,  $LiB_2C_2$  (75 K),  $NaB_2C_2$  (81 K),  $KB_2C_2$  (102 K),  $CaB_2C_2$  (88 K),  $SrB_2C_2$  (91 K), and  $LaB_2C_2$  (94 K). Based on comprehensive analysis of the electronic and vibrational properties, we propose two key descriptors for filtering and diagnosing high- $T_c$   $MB_2C_2$  films: one involving  $\sigma$  electrons of covalent B-C bonds driven metallic and the other focusing on large deformation potentials for  $\sigma$  bands near the Fermi level originating from frozen-in in-plane B-C bond-stretching modes at the zone center. Utilizing two descriptors, we expediently identify the  $KLaB_4C_4$  film as a potential high- $T_c$  candidate (70 K) among 15 bimetal borocarbides. These findings provide valuable insights into the electronic and vibrational properties that contribute to enhanced superconducting behavior, aiding in the design and discovery of new 2D materials with the potential to break the  $T_c$  record for conventional superconductivity.

DOI: [10.1103/PhysRevB.110.064513](https://doi.org/10.1103/PhysRevB.110.064513)

### I. INTRODUCTION

While significant progress has been made in discovering new superconducting materials with higher critical temperatures  $T_c$  [1–20], the goal of room-temperature superconductivity remains elusive. Theoretical and experimental studies have suggested that highly compressed superhydrides could potentially exhibit superconductivity at or near room temperature, exemplified by  $H_3S$  [3–5],  $CaH_6$  [6–8],  $LaH_{10}$  [9–13], etc. However, the challenge lies in stabilizing these superconducting phases under ambient pressure conditions.

In the pursuit of high- $T_c$  conventional superconductors under ambient pressure, light-element-based materials, especially those incorporating boron and carbon elements, have emerged as prominent candidates [21–40], represented by  $MgB_2$  (39 K) [21,22], B-doped Q-carbon (55 K) [23,24], and  $SrB_3C_3$  (43 K) [25–28]. The outstanding superconducting properties of these materials are underpinned by a shared characteristic, namely, the presence of doped  $sp^3$ - or  $sp^2$ -hybridized  $\sigma$ -bonding covalent bonds. These partially filled electronic states result in a substantial density of states (DOS) at the Fermi level. Additionally, the strong B-B and B-C bonds exhibit rigid vibrational modes that resist significant softening caused by strong electron-phonon coupling (EPC). The superconductivity in these compounds is mainly attributed to

the coupling between  $\sigma$ -bonding electrons and lattice vibrations, offering valuable insights for searching for potential high- $T_c$  candidates. Numerous endeavors have been dedicated to exploring such compounds, with a particular focus on the analogs of bulk  $MgB_2$  [29–37]. For example, hole-doped lithium borocarbide (LiBC) has been predicted to be a possible high- $T_c$  candidate ( $\sim 100$  K for  $Li_{0.5}BC$ ) [29]. Other compounds, including  $Li_3B_4C_2$  and  $Li_2B_3C$ , could become superconducting above 50 K [30]. Similar compounds also include  $MgBC$  (51 K) [31] and  $MgB_3C_3$  (59 K) [32]. However, the challenge regarding the thermodynamic stability of these materials remains a significant obstacle [32,41–43].

Two-dimensional (2D) materials provide a promising solution to the thermodynamic stability challenges encountered by bulk materials. They can be obtained by exfoliating layers from bulk parent compounds or by utilizing molecular beam epitaxy to grow them on suitable metal substrates, particularly when parent compounds are unavailable. Consequently, the 2D analogs of bulk  $MgB_2$  [44–53] have recently garnered considerable attention due to their possibility of synthesis and the potential for high superconductivity. Theoretical studies suggested that the hydrogenated  $MgB_2$  monolayer has a high  $T_c$  of 67 K, which can be further boosted to over 100 K by applying biaxial strain [46]. Other  $MgB_2$ -like 2D materials— $(Al, In)B_2$  (27, 42 K) [47,48],  $(Li, Be, Mg, Al, Zn, Ga, Ge, In)B_4$  (32–53 K) [47–49],  $LiBC$  (70 K) [50],  $(Li, Ca)B_2C_2$  (92, 97 K) [51,52], and  $Mg_2B_4C_2$  (48 K) [53]—have been predicted to superconduct at a strikingly high  $T_c$ . EPC analysis indicates a similarity in the superconducting mechanism and multigap

<sup>\*</sup>Contact author: [xml@calypso.cn](mailto:xml@calypso.cn)

<sup>†</sup>Contact author: [yinwei\\_li@jsnu.edu.cn](mailto:yinwei_li@jsnu.edu.cn)

superconducting character between  $\text{MgB}_2$  and these materials [22,45–52]. We note that 2D metal borocarbides ( $\text{MB}_2\text{C}_2$ ) exhibit higher  $T_c$  compared to the corresponding metal borides due to more softened vibration modes resulting from zone-centered in-plane bond-stretching phonon. However, current research on superconducting 2D metal borocarbides is in its early stages, and only  $\text{LiB}_2\text{C}_2$  [51] and  $\text{CaB}_2\text{C}_2$  [52] have been confirmed, limiting the discovery of new high- $T_c$  2D materials.

To screen for high- $T_c$   $\text{MB}_2\text{C}_2$  films and gain a comprehensive understanding of their coupling mechanism, we carried out high-throughput EPC calculations. Six potential superconducting candidates with  $T_c \geq 75$  K were identified, and the highest  $T_c$  of 102 K in  $\text{KB}_2\text{C}_2$  was predicted. Note that we have established two critical criteria to prejudge the high- $T_c$   $\text{MB}_2\text{C}_2$  films based on their superconducting mechanism. The first one is the  $sp^2$ -hybridized  $\sigma$ -bonding bands driven metallic. The second one is the large deformation potentials for  $\sigma$  bands resulting from frozen-in interlayer bond-stretching modes at the  $\Gamma$  point. Following these two criteria, the  $\text{KLaB}_4\text{C}_4$  film has been identified as a potential high- $T_c$  candidate with a  $T_c$  of 70 K among the 15 bimetal borocarbides ( $\text{M1M2B}_4\text{C}_4$ ).

## II. COMPUTATIONAL DETAILS

The structural relaxations and electronic structure calculations were performed based on density functional theory [54] with the implementation of the Vienna *Ab initio* Simulation Package (VASP) [55,56]. The Perdew-Burke-Ernzerhof generalized gradient approximation [57] was chosen for the exchange-correlation function. The electron-ion interactions were considered by the projector augmented-wave potentials [58]. A plane-wave cutoff energy of 600 eV and Monkhorst-Pack  $k$  meshes [59] with a grid of  $20 \times 20 \times 1$  were adopted to give energy and force convergence precisions of  $10^{-6}$  eV and  $0.01$  eV  $\text{\AA}^{-1}$ , respectively. A vacuum  $\sim 20$   $\text{\AA}$  thick was used to eliminate the periodic interactions along the  $c$  axis. The phonon spectra and EPC were calculated within density functional perturbation theory [60] using the QUANTUM ESPRESSO code [61]. Ultrasoft pseudopotentials [62] were used to model the electron-ion interactions. The kinetic energy cutoffs for wave functions and charge density were chosen to be 80 and 800 Ry, respectively. A  $k$ -point mesh of  $24 \times 24 \times 1$  ( $16 \times 32 \times 1$ ) and a  $q$ -point mesh of  $12 \times 12 \times 1$  ( $8 \times 16 \times 1$ ) in the first Brillouin zone were used in the phonon calculations for  $\text{MB}_2\text{C}_2$  ( $\text{M1M2B}_4\text{C}_4$ ) films. We employed the Electron-phonon Wannier (EPW) code [63–65] for the superconducting gap and EPC and the WANNIER90 code [66] for generating maximally localized Wannier functions (MLWFs). An interpolated  $k$ -point grid of  $240 \times 240 \times 1$  ( $80 \times 160 \times 1$ ) and a  $q$ -point grid of  $120 \times 120 \times 1$  ( $40 \times 80 \times 1$ ) were adopted to interpolate the EPC quantities of  $\text{MB}_2\text{C}_2$  ( $\text{M1M2B}_4\text{C}_4$ ) films. The fermion Matsubara frequency cutoff was set to be 1.0 eV, which is  $\sim 8$  times larger than the largest phonon frequency. The width of the Fermi surface window was set at 0.2 eV. Dirac  $\delta$  functions for electrons and phonons were smeared out by Gaussian functions with widths of 50 and 0.2 meV, respectively. The Morel-Anderson pseudopotential  $\mu_c^*$  is a semiempirical parameter to solve the numerical

solution of the Eliashberg equation, defined as  $\mu_c^* = \mu^*/[1 + \mu^* \ln(\omega_{\text{el}}/\omega_{\text{ph}})]$  [67], where  $\omega_{\text{el}}$  and  $\omega_{\text{ph}}$  are the characteristic electron and phonon energies, respectively, and  $\mu^*$  is the Coulomb potential. Here we adopt  $\mu^* = 0.13$  and the resulting  $\mu_c^* = 0.18$ . The convergence test of superconducting gaps, the EPC constant, and the consistency of band structures obtained by MLWFs interpolation and first-principles calculations are given in Figs. S1–S8 in the Supplemental Material (SM) [68].

## III. RESULTS AND DISCUSSION

Figure 1(a) illustrates the band structure and the projected density of states (PDOS) of two honeycomb BC layers, where the B and C atoms are arranged alternately. Two distinct sets of bands can be identified: the hybridized  $sp^2$  ( $\sigma$ ) states and the unhybridized  $p_z$  ( $\pi$ ) states. Both sets of states are partially filled, indicating a metallic nature for the  $\text{B}_2\text{C}_2$  film. There is a higher density of electron carriers in the  $\pi$  bands than in the  $\sigma$  states. The electronic characteristics observed in the  $\text{B}_2\text{C}_2$  film have similarities to those found in bulk  $\text{MgB}_2$ , suggesting a potential for comparable superconducting behavior. However, phonon spectra calculations reveal the lack of dynamical stability in the  $\text{B}_2\text{C}_2$  film due to the electron-deficiency nature (Fig. S9 in the SM [68]).

The effectiveness of metal intercalation has been demonstrated for stabilizing 2D crystal structures [44–53,69–73]. Li and Ca intercalated honeycomb BC layers have been studied. Gao *et al.* reported that  $\text{LiB}_2\text{C}_2$  is a good candidate for realizing high- $T_c$  (92 K) superconductivity by solving the anisotropic Eliashberg equations [51]. Liu *et al.* revealed surface superconductivity with a  $T_c$  of  $\sim 90$  K in  $\text{Ca}_n\text{B}_{n+1}\text{C}_{n+1}$  ( $n = 1, 2, 3, \dots$ ) films [52]. Metal intercalators can introduce additional charge carriers into the system, modifying its electronic structure and properties [72,73]. The extent of these alterations depends on factors such as the valence of the intercalated metal atom, the degree of charge transfer, and the interaction between the intercalant and the system.

To investigate the impact of intercalation on the electronic properties of the  $\text{B}_2\text{C}_2$  film, we conducted electronic property calculations using representative intercalants: Li, Mg, Ca, Sc, and La, as shown in Figs. 1(b)–1(f). In the case of full electron transfer from the bivalent Mg, the resulting formula is  $\text{M}^{2+}[\text{B}_2\text{C}_2]^{2-}$ , leading to an insulating state. When the valence of the intercalated metal is less than +2, it results in hole-doped metals. Conversely, when the valence of the metal is greater than +2, it leads to electron-doped metals. Typically, the band structures exhibit rigid band behavior when the interaction between the intercalant and  $\text{B}_2\text{C}_2$  film is weak [Figs. 1(b) and 1(c)]. However, in the case of bivalent Ca, the Ca  $d$  orbitals exhibit stronger hybridization with the  $\pi$  orbitals compared to the  $\sigma$  orbitals near the Fermi level, lowering the  $\pi$  bands, resulting in a  $\sigma$  to  $\pi$  charge transfer, which further drives hole doping of the  $\sigma$  bands [Fig. 1(d)]. The related conclusions about the band structure are demonstrated by  $\text{MgB}_2$  [74]. Compared to Sc [Fig. 1(e)], La transfers fewer electrons into  $\text{B}_2\text{C}_2$  (Table SI in the SM [68]). As a result, the  $\sigma$  states remain partially unfilled [Fig. 1(f)].

How do the valence states of metal atoms and the interactions between metal atoms and  $\text{B}_2\text{C}_2$  influence the structural

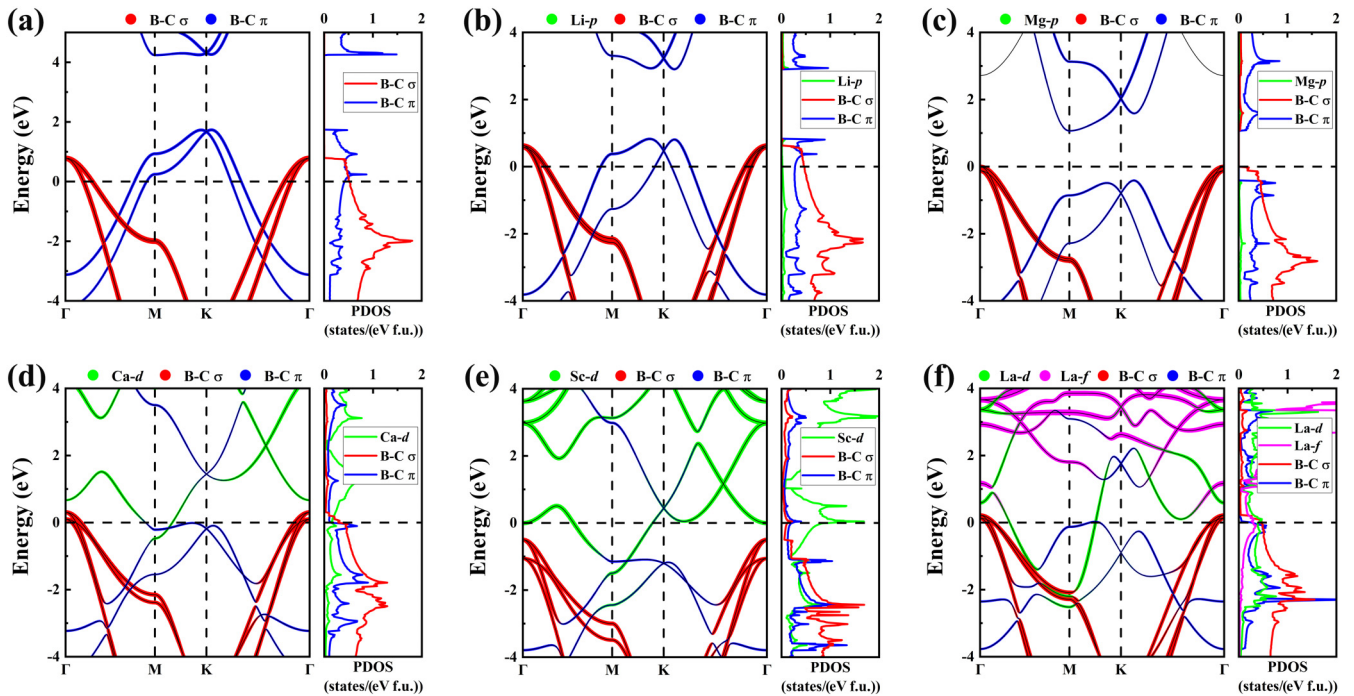


FIG. 1. The orbital-resolved band structures and the projected density of states (PDOS) of (a) pristine  $B_2C_2$ , (b)  $LiB_2C_2$ , (c)  $MgB_2C_2$ , (d)  $CaB_2C_2$ , (e)  $ScB_2C_2$ , and (f)  $LaB_2C_2$  films.

stability, electronic properties, and superconducting properties of  $MB_2C_2$  films? To answer this question we carried out high-throughput first-principles calculations of the  $MB_2C_2$  family. An overview of the screening strategy for exploring 2D high- $T_c$   $MB_2C_2$  compounds is outlined in Fig. 2(a). We performed full structure optimization for 41 metal intercalation compounds rather than assuming universal lattice constants and assessed their dynamical stabilities through phonon calculations. Among them, 23 were identified as dynamically stable (Figs. S10–S17 in the SM [68]). Within these

23 compounds, 21 exhibited metallic properties according to their band structures (Figs. S10–S17 in the SM [68]). Furthermore, out of these 21 metallic compounds, 4 were found to be magnetic (Fig. S10 in the SM [68]). Ultimately, we obtained 17 stable nonmagnetic metallic phases [Fig. 2(b)]. The van der Waals interactions [75] have negligible influence on the geometry of dynamically stable  $MB_2C_2$  films (Table SII in the SM [68]).

By thoroughly solving anisotropic Migdal-Eliashberg equations, we identified  $MB_2C_2$  films including  $M = Li, Na,$

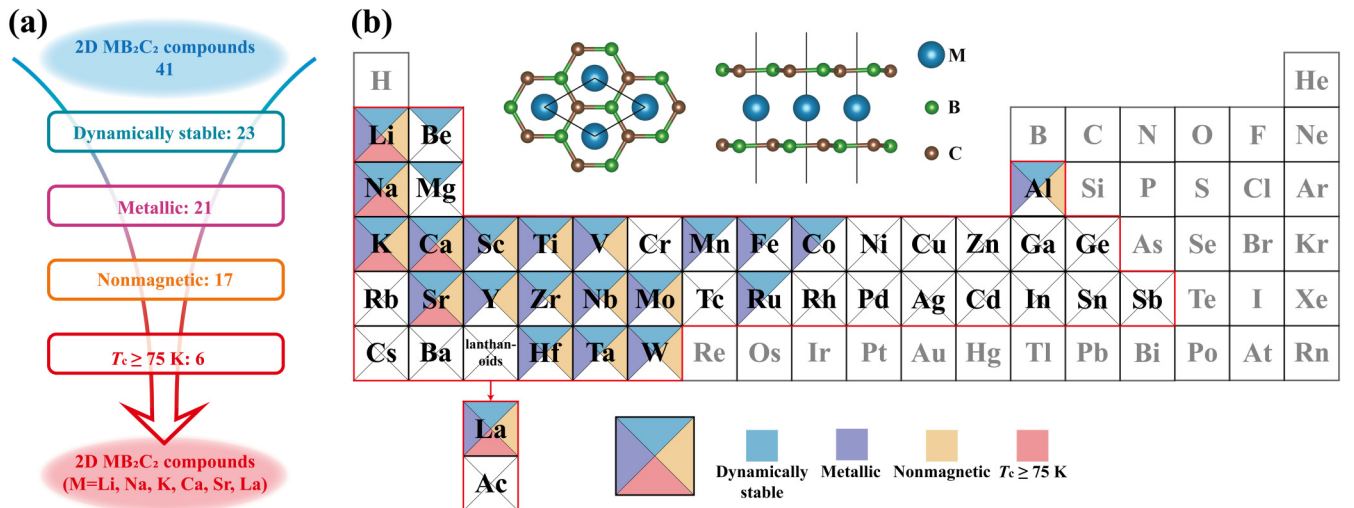


FIG. 2. (a) Schematic diagram of the screening procedure for high- $T_c$   $MB_2C_2$  films. (b) Results of high-throughput calculations of phonon dispersion curves, electronic properties, magnetic properties, and EPC calculations for  $MB_2C_2$  films, where  $M$  represents the 41 metal elements in the red frame. The inset shows the 2D crystal structure for  $MB_2C_2$ .



TABLE I. The total electron density of states at the Fermi level  $N(E_F)$  [states/(eV/f.u.)], density of states of  $\sigma$  electrons at the Fermi level  $N(E_F)_\sigma$  [states/(eV/f.u.)], logarithmic frequency average  $\omega_{\log}$  (K), degree of  $E_g$  phonon mode softening at the zone center  $\tilde{\omega} - \omega$  (THz), deformation potentials for  $\sigma$  bands from a frozen-in  $E_g$  mode  $\mathcal{D}_{E_g}$  (eV/Å), EPC constant  $\lambda$ , superconducting critical temperature calculated by the anisotropic Migdal-Eliashberg theory  $T_c^{\text{ME}}$  (K), Allen-Dynes modified McMillan equation  $T_c^{\text{AD}}$  (K), and distance from the convex hull  $\Delta H$  (meV/atom) of high- $T_c$   $MB_2C_2$  films. Note that the thermodynamic stability analysis of these high- $T_c$  compounds could be found in Appendix A.

Compound	$N(E_F)$	$N(E_F)_\sigma$	$\omega_{\log}$	$\tilde{\omega} - \omega$	$\mathcal{D}_{E_g}$	$\lambda$	$T_c^{\text{ME}}$ ( $\mu_c^* = 0.18$ )	$T_c^{\text{AD}}$ ( $\mu^* = 0.13$ )	$\Delta H$
LiB <sub>2</sub> C <sub>2</sub>	0.76	0.46	646.29	8.22	19.10	1.03	75	35	0
NaB <sub>2</sub> C <sub>2</sub>	1.11	0.50	487.76	11.26	18.40	1.37	81	47	0
KB <sub>2</sub> C <sub>2</sub>	0.88	0.49	566.84	10.17	17.90	1.81	102	49	62
CaB <sub>2</sub> C <sub>2</sub>	0.61	0.28	567.27	5.44	17.10	1.38	88	35	0
SrB <sub>2</sub> C <sub>2</sub>	2.40	0.48	388.51	12.24	17.00	2.02	91	39	99
LaB <sub>2</sub> C <sub>2</sub>	1.54	0.46	388.05	8.74	16.10	1.14	94	20	0

K, Ca, Sr, and La as potential two-gap high- $T_c$  superconductors with  $T_c$  of 75–102 K (Table I). Notably, the KB<sub>2</sub>C<sub>2</sub> film demonstrated the highest  $T_c$  of 102 K. We emphasize that the estimated  $T_c$  of  $MB_2C_2$  films based on the Allen-Dynes modified McMillan equation are lower than those derived from the full anisotropic Migdal-Eliashberg equation, especially for these anisotropic superconductors (Table I and Table SIII in the SM [68]). This situation was commonly seen in previous studies, for example,  $\sim 50.0$  K in MgB<sub>2</sub> [65] derived from the anisotropic Migdal-Eliashberg equation, which is higher than that (24.8 K for MgB<sub>2</sub> [44]) calculated by the Allen-Dynes modified McMillan equation. Given the similarities in the superconducting behaviors across these high- $T_c$   $MB_2C_2$  superconductors, we focus on the representative KB<sub>2</sub>C<sub>2</sub> film for an in-depth examination of the underlying superconducting mechanism.

The intercalated K atom in the KB<sub>2</sub>C<sub>2</sub> film possesses a valence of +1, leading to hole-doping driven metallicity. The weak interaction between K and the B<sub>2</sub>C<sub>2</sub> film has a minimal effect on the overall shape of the film's electronic bands but can lift the position of the Fermi level. Consequently, KB<sub>2</sub>C<sub>2</sub> is expected to exhibit a rigid band behavior in comparison to the pristine B<sub>2</sub>C<sub>2</sub> film. As illustrated in Fig. 3(a), for KB<sub>2</sub>C<sub>2</sub>, four bands across the Fermi level have partially filled  $\sigma$  and  $\pi$  states. In comparison to the  $\pi$ -bonding electrons, the  $\sigma$ -bonding electrons make a slightly larger contribution at the Fermi level. The Fermi surface can be divided into two independent sheets based on the distributions of  $\sigma$  and  $\pi$  orbitals [Fig. 3(b)]. The  $\sigma$  electrons are primarily concentrated in two small circles around the  $\Gamma$  point, while the  $\pi$  electrons are predominantly located in a larger circle surrounding the  $\Gamma$  point and the sheets around the  $K$  point. This anisotropic distribution of the orbital character on the Fermi surface is naturally anticipated to result in a multigap superconducting nature in the KB<sub>2</sub>C<sub>2</sub> film, as the distinct  $\sigma$  and  $\pi$  bands can support different superconducting gaps.

Figure 3(c) shows the  $\lambda_{qv}$ -weighted phonon spectrum, the Eliashberg spectral functions  $\alpha^2F(\omega)$ , and the integrated EPC strength  $\lambda(\omega)$  in the KB<sub>2</sub>C<sub>2</sub> film. Figure 3(d) shows the vibrational patterns of strongly coupled phonon modes. The absence of any imaginary frequencies confirms the dynamical stability of the KB<sub>2</sub>C<sub>2</sub> film. The low-frequency phonon branches below 200 cm<sup>-1</sup> are dominated by the vibrations of

K atoms, and the high-frequency parts arise from the vibrations of the B-C layers. At the  $\Gamma$  point, two strongly coupled phonon modes,  $E_g$  and  $E_u$ , exclusively involving the in-plane vibrations of B-C layers [Fig. 3(d)] exist. The frequencies of the  $E_u$  and  $E_g$  modes are 593 and 606 cm<sup>-1</sup>, respectively, which are  $\sim 8\%$  and 10% higher than the frequency of the  $E_{2g}$  modes in MgB<sub>2</sub> [33]. This enhancement can be attributed to the increased strength of B-C  $\sigma$  bonds in comparison to B-B  $\sigma$  bonds. Besides these two modes, several low-frequency phonon modes also make a sizable contribution to  $\lambda_{qv}$ , such as the  $A_g$  and  $B_u$  modes around 260 cm<sup>-1</sup> at the  $M$  point, which involve only the out-of-plane vibrations of B-C layers [Fig. 3(d)]. The primary peak of  $\alpha^2F(\omega)$  from 470 to 610 cm<sup>-1</sup> results from  $E_g$  and  $E_u$  modes. A second primary peak of  $\alpha^2F(\omega)$  around 260 cm<sup>-1</sup> is contributed by  $A_g$  and  $B_u$  modes.

The deformation potential, denoted as  $\mathcal{D} \equiv \Delta_{\varepsilon_k}/\Delta_Q$ , serves as a straightforward method to identify strong EPC, where  $\varepsilon_k$  is the energy of electronic states and  $Q$  is the frozen-in phonon mode amplitudes [76]. The fundamental idea is that a phonon mode exhibiting strong coupling with electronic states at the Fermi surface will induce a significant shift in the electronic band  $\varepsilon_k$  near the Fermi level [76]. We adopted a root-mean-square displacement of  $\Delta_u = 0.057$  Å (the same parameter as used in Ref. [74]) to provide a clear picture of the substantial effect of EPC strength. Figures 3(e) and 3(f) depict the band structures of the KB<sub>2</sub>C<sub>2</sub> film with frozen-in  $E_g$  and  $A_g$  modes, respectively. The frozen-in  $E_g$  phonon mode significantly splits the  $\sigma$  band, creating a gap  $\Delta_{\varepsilon_{\text{gap}}}$  of  $\sim 2$  eV at the  $\Gamma$  point and subsequently resulting in a deformation potential ( $\Delta_{\varepsilon_{\text{gap}}}/\Delta_u = 2\mathcal{D}_{E_g}$ ) of  $\sim 18$  eV/Å. Notably, the deformation potential in the KB<sub>2</sub>C<sub>2</sub> film is larger than that in MgB<sub>2</sub> ( $\mathcal{D}_{E_{2g}} = 13$  eV/Å) [74], indicating a stronger EPC strength in the KB<sub>2</sub>C<sub>2</sub> film. The EPC constant  $\lambda$  of the KB<sub>2</sub>C<sub>2</sub> film is calculated to be 1.81,  $\sim 2.5$  times higher than that of MgB<sub>2</sub> [33]. The  $A_g$  mode induces a gap opening of  $\sim 0.07$  eV in the  $\pi$  bands at the  $K$  point [Fig. 3(f)]. The corresponding deformation potential  $\mathcal{D}_{A_g}$  is  $\sim 15$  times smaller than  $\mathcal{D}_{E_g}$ , highlighting the negligible coupling strength associated with the  $A_g$  mode. Our results underscore the significant impact of the lattice vibrations on the electronic structures, which is a crucial aspect of the superconducting mechanism.

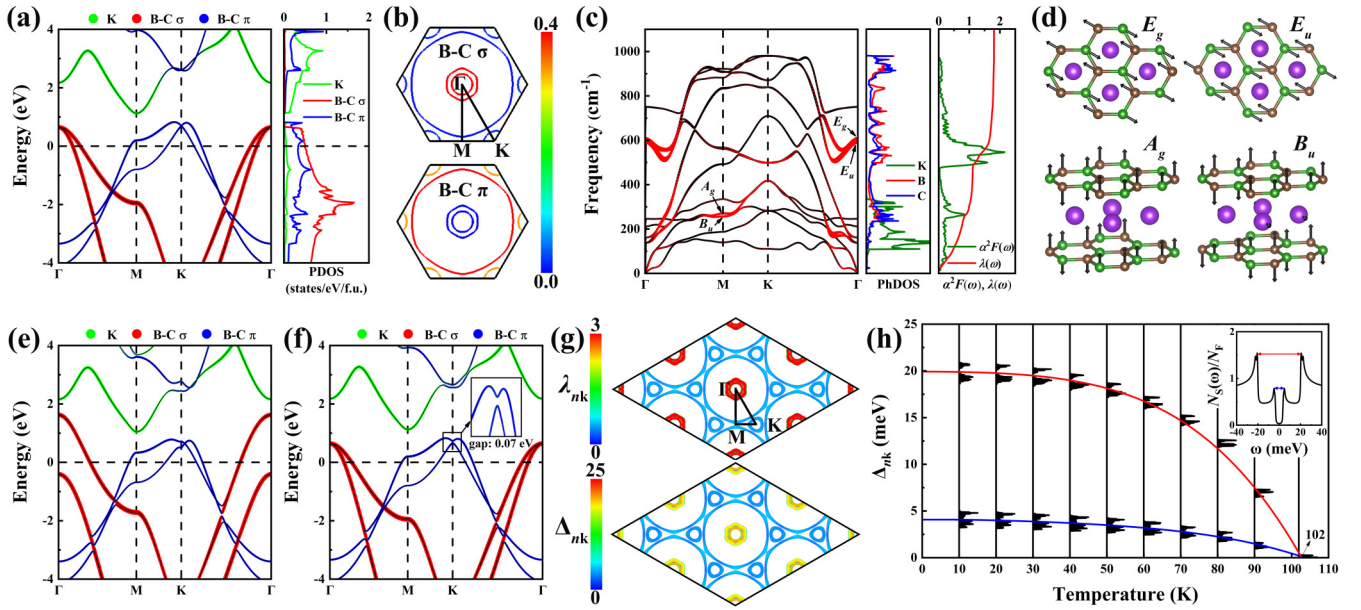


FIG. 3. (a) The orbital-resolved band structure and PDOS of the  $\text{KB}_2\text{C}_2$  film. (b) The distribution of B-C  $\sigma$  and  $\pi$  orbitals on the Fermi surface using the color scale in the range  $[0, 0.4]$ . A greater contribution of B-C  $\sigma$  or  $\pi$  electrons in a certain region of the Fermi surface corresponds to values closer to 0.4, with the color tending towards red. Conversely, a smaller contribution of B-C  $\sigma$  or  $\pi$  electrons corresponds to values closer to 0, with the color tending towards blue. (c) Phonon dispersion relations, projected phonon density of states (PhDOS), Eliashberg function  $\alpha^2 F(\omega)$ , and integrated EPC strength  $\lambda(\omega)$  of  $\text{KB}_2\text{C}_2$ . The size of the red dots represents phonon linewidth, which indicates the strength of interactions between phonons and electrons. (d) Vibrational patterns for the  $E_g$ ,  $E_u$ ,  $A_g$ , and  $B_u$  phonon modes, with black arrows indicating the atomic vibration direction. The distinction between  $E_g$  and  $E_u$  modes lies in the relative alignment of the in-plane vibration directions of the two layers. For the  $E_g$  mode, the in-plane vibration directions of both layers are aligned, resulting in a symmetric vibrational pattern. On the other hand, for the  $E_u$  mode, the in-plane vibration directions of the two layers are misaligned. One layer aligns with the  $E_g$  mode, while the other layer has a different vibration direction, leading to an antisymmetric vibrational pattern between the layers. (e) and (f) Band structures with frozen-in  $E_g$  and  $A_g$  modes, respectively, which are plotted along the same lines as in (a) to facilitate comparison (note that the point labeled  $K$  is no longer a symmetry point for the  $E_g$  mode). (g) The momentum-resolved EPC  $\lambda_{nk}$  and the superconducting gaps  $\Delta_{nk}$  ( $T = 10$  K) of  $\text{KB}_2\text{C}_2$  on the Fermi surface. (h) Energy distribution of superconducting gaps  $\Delta_{nk}$  versus  $T$  for  $\text{KB}_2\text{C}_2$ . The inset refers to the density of states in the superconducting state calculated at  $T = 10$  K, showing the overall two-gap nature as well as the anisotropy of the gap spectrum.

Figure 3(g) shows the distribution of superconducting energy gaps  $\Delta_{nk}$  and momentum-resolved EPC  $\lambda_{nk}$  on the Fermi surface. The Fermi surface exhibits two anisotropic superconducting gaps, which correspond to the  $\sigma$  bands and the  $\pi$  bands. This two-gap superconductivity arises from the anisotropic nature of the EPC constant  $\lambda_{nk}$  in different Fermi sheets. At 10 K [Fig. 3(h)], the Fermi surface gaps of  $\Delta_\sigma$  and  $\Delta_\pi$  range from 18.5 to 21.0 and 3.1 to 5.0 meV, respectively. These gap values are larger than those ( $\Delta_\sigma = 7.0$ – $7.1$  meV and  $\Delta_\pi = 2.3$ – $2.8$  meV) measured in  $\text{MgB}_2$  at 4.2 K [77–79]. The temperature at which the superconducting gap vanishes indicates a  $T_c$  of 102 K in the  $\text{KB}_2\text{C}_2$  film. The high  $T_c$  is attributed to the strong coupling between the  $\sigma$  electrons and the  $E_g$  phonon modes.

Based on the overall analysis of the electronic properties, vibrational properties, and coupling mechanism across 17  $\text{MB}_2\text{C}_2$  films (as depicted in Figs. S10–S22 in the SM [68]), we propose two important and simple descriptors that are rooted in distinct physical intuitions. Descriptor 1 states that the presence of metallic behavior is driven by the  $\sigma$  electrons. Specifically, the valence of the intercalated metal should be equal to or less than +3 to effectively serve as an electron donor [Fig. 4(a)]. Descriptor 2 is the softening of  $E_g$  phonon modes (Table I and Table SIII in the SM [68]). The softening

of the  $E_g$  phonon modes is correlated with larger deformation potentials  $D_{E_g}$  observed for the  $\sigma$  bands near the Fermi level (Table I, Fig. 4(b), and Fig. S23 in the SM [68]). The two descriptors provide physical insights into the electronic properties, vibrational properties, and their coupling in 2D  $\text{MB}_2\text{C}_2$  systems. The strong coupling between the  $\sigma$  electrons and the  $E_g$  phonon modes is highlighted as an important factor in promoting superconducting behavior and enhancing the superconductivity in  $\text{MB}_2\text{C}_2$  films.

Delving into the rules more deeply, we further explore potential high- $T_c$  bimetal borocarbides ( $M1M2B_4C_4$ ) in which the average valence of the bimetal atoms is less than or equal to +3. Specifically, we consider combinations with  $M1M2 = \text{LiSc}, \text{LiY}, \text{LiLa}, \text{NaSc}, \text{NaY}, \text{NaLa}, \text{KSc}, \text{KY}, \text{KLa}, \text{CaTi}, \text{CaZr}, \text{CaHf}, \text{SrTi}, \text{SrZr}, \text{and SrHf}$ . Figure 5(a) demonstrates that out of the 15  $M1M2B_4C_4$  compounds examined, only 6 were dynamically stable. Within this subset, it is notable that only the compound  $\text{KLaB}_4\text{C}_4$  satisfies both descriptors. This suggests that  $\text{KLaB}_4\text{C}_4$  has the potential to exhibit high- $T_c$  superconductivity. The band structure of  $\text{KLaB}_4\text{C}_4$  demonstrates  $\sigma$  electrons driven metallic [Fig. 5(b)]. The  $\lambda_{qv}$ -weighted phonon spectrum suggests that the two strongly coupled phonon modes,  $A_g$  and  $B_u$  [Fig. 5(c)], mainly involve the in-plane vibrations of B-C layers (Fig. S24 in the SM

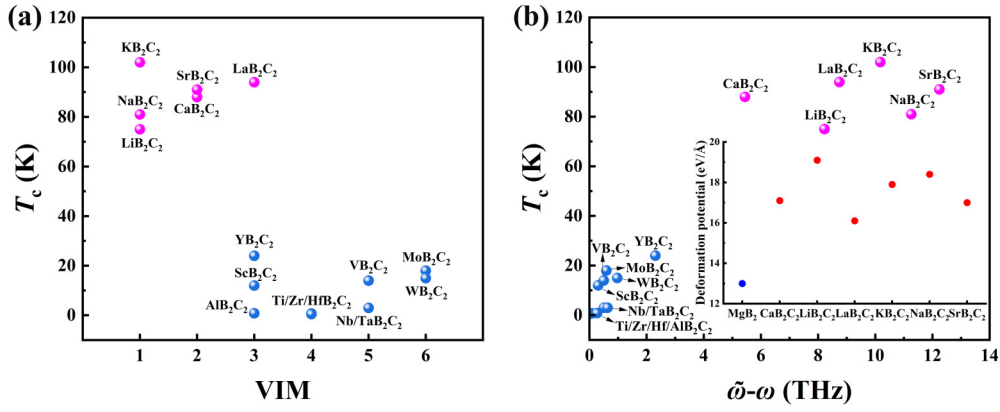


FIG. 4.  $T_c$  of  $MB_2C_2$  films versus (a) the valence of the intercalated metal (VIM) and (b) the  $E_g$  phonon softened value calculated by determining the difference between the unscreened ( $\tilde{\omega}$ ) and screened ( $\omega$ ) phonon frequencies at the zone center [80]. The softening of the  $E_g$  phonon mode is indicative of strong EPC, which is a crucial factor for high- $T_c$  superconductivity. The inset in (b) shows the deformation potentials for  $\sigma$  bands from the frozen-in  $E_g$  mode in high- $T_c$   $MB_2C_2$  ( $M = Li, Na, K, Ca, Sr,$  and  $La$ ) films.

[68]). By thoroughly solving anisotropic Migdal-Eliashberg equations, we predict that  $KLaB_4C_4$  film has a  $T_c$  of 70 K [Fig. 5(d)]. As a comparison, we also conducted EPC calculations for the  $NaScB_4C_4$  film, which is not anticipated to exhibit a significant EPC based on our rules. Our results indicate a value of  $\lambda = 0.36$  and a  $T_c$  of  $< 1$  K for  $NaScB_4C_4$  (Fig. S25 in the SM [68]).

#### IV. CONCLUSION

In summary, we conducted high-throughput first-principles calculations to explore  $MgB_2$ -like 2D materials— $MB_2C_2$  films, where  $M$  represents 41 different metal elements. Out of these 41 metals, we found that 23 films were dynamically stable. Furthermore, we identified six potential superconducting candidates with  $T_c \geq 75$  K. The highest predicted  $T_c$  of

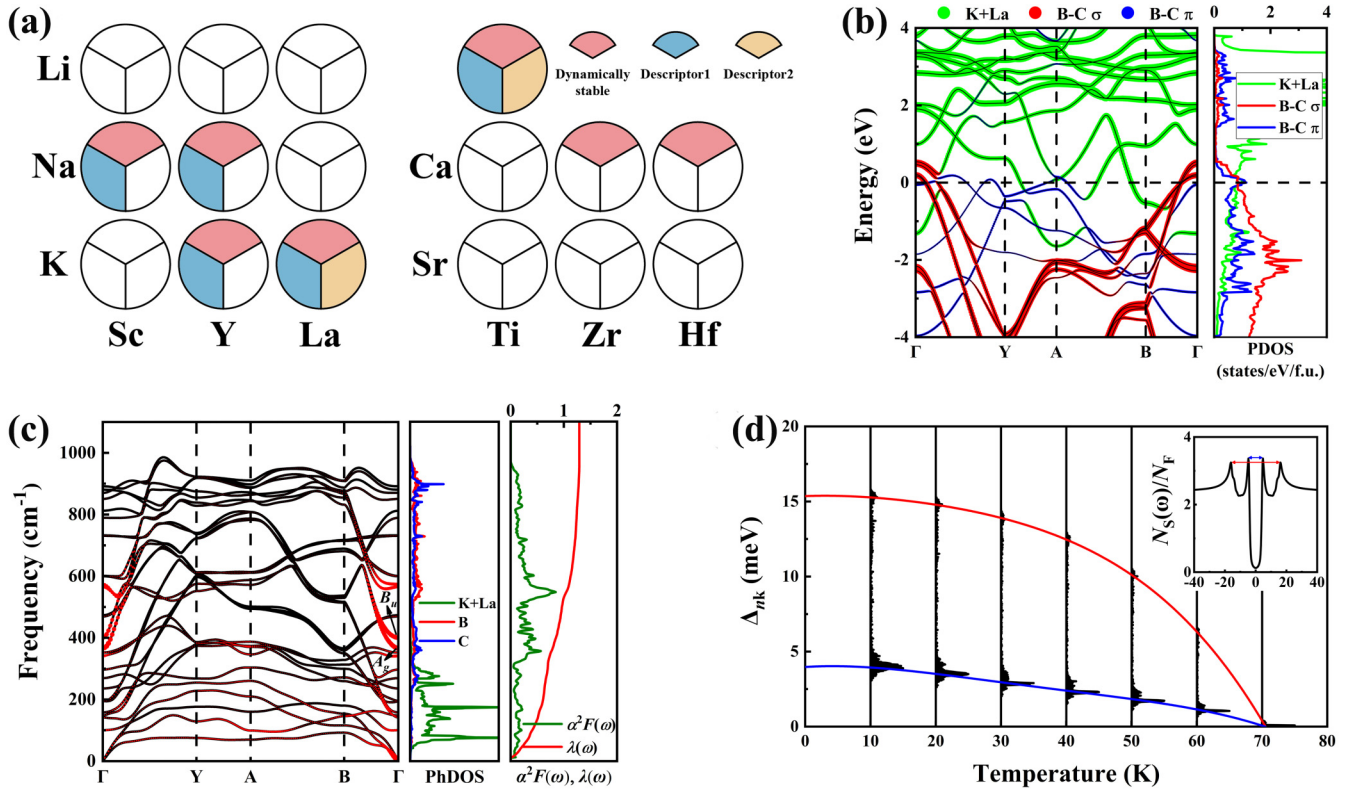


FIG. 5. (a) Schematics of applying two key descriptors to screen for high- $T_c$   $M1M2B_4C_4$  films. (b) The orbital-resolved band structure and PDOS of the  $KLaB_4C_4$  film. (c) Phonon dispersion relations, projected phonon density of states (PhDOS), Eliashberg function  $\alpha^2 F(\omega)$ , and integrated EPC strength  $\lambda(\omega)$  of the  $KLaB_4C_4$  film. (d) Energy distribution of superconducting gaps  $\Delta_{nk}$  versus  $T$  for the  $KLaB_4C_4$  film. The inset shows the density of states in the superconducting state calculated at  $T = 10$  K, showing the two-gap superconducting nature.



102 K was found in the  $\text{KB}_2\text{C}_2$  film. The metal atoms in these  $\text{MB}_2\text{C}_2$  films act as electron donors to the  $\text{B}_2\text{C}_2$  layers, influencing the number of occupied states at the Fermi level. Based on our comprehensive analysis of the electronic and vibrational properties of numerous  $\text{MB}_2\text{C}_2$  films, we established two key descriptors that are indicative of high superconductivity. One important descriptor is the presence of metallic behavior driven by the  $\sigma$ -bonding bands in the material. The second descriptor is the observation of optical phonon softening, specifically derived from the in-plane bond-stretching vibrations. Applying the two descriptors, we efficiently identified  $\text{KLaB}_4\text{C}_4$  as a potential high- $T_c$  candidate among the 15 bimetal borocarbides ( $M1M2B_4C_4$ ), with a predicted  $T_c$  of 70 K. These findings contribute to the understanding of superconducting mechanisms in this class of materials and facilitate the targeted exploration of novel 2D high- $T_c$  materials.

### ACKNOWLEDGMENTS

The authors acknowledge funding support from the National Natural Science Foundation of China under Grants No. 12374010, No. 12074154, No. 11904142, and No. 11722433; the Six Talent Peaks Project; the 333 High-level Talents Project of Jiangsu Province; and the Postgraduate Research & Practice Innovation Program of Jiangsu Province under Grant No. KYCX23\_2901. Computational resources were provided by the High-Performance Computing Center of the School of Physics and Electronic Engineering of Jiangsu Normal University.

### APPENDIX A: THE THERMODYNAMIC STABILITY OF HIGH- $T_c$ $\text{MB}_2\text{C}_2$ FILMS

We performed structure searches for  $\text{LiB}_2\text{C}_2$ ,  $\text{NaB}_2\text{C}_2$ , and  $\text{KB}_2\text{C}_2$  films (involving 2 f.u. at most) using the Crystal structure AnaLYsis by Particle Swarm Optimization (CALYPSO) method [81–85], which is a powerful tool for structural predictions, allowing us to thoroughly explore the potential energy surface and identify the global minimum structures. Our structure searches successfully reproduced the  $\text{MB}_2\text{C}_2$  films studied in this paper but also identified a different energy-degenerate structure. The difference between the two structures is the stacking arrangement of two honeycomb BC layers: the original structure has AB stacking, while the other structure has AA stacking. Considering that the energy difference between the two structures is so small, as shown in Table SIV in the SM [68], with some differences being less than 1 meV/atom, this consequently indicates a relatively flat potential energy surface in the vicinity of the global minimum. This flat energy landscape suggests the possibility of the two structures coexisting. Additionally, the two phases exhibit essentially the same electronic properties, suggesting that either structure could be a viable candidate for high- $T_c$  superconducting  $\text{MB}_2\text{C}_2$  films. In the paper, we focus on the AB-stacked  $\text{MB}_2\text{C}_2$  films because of the existence of this stacking style in bulk materials.

The thermodynamic stability of the  $\text{MB}_2\text{C}_2$  materials was evaluated by constructing the convex hulls of the  $M$ -B-C ternary system. A total of seven different compositions, including  $\text{MBC}$ ,  $\text{MB}_2\text{C}_2$ ,  $\text{MB}_3\text{C}_3$ ,  $\text{MB}_4\text{C}_4$ ,  $\text{MB}_6\text{C}_6$ ,  $\text{MB}_4\text{C}_8$ , and  $\text{MB}_2\text{C}_{10}$  (Fig. S26 in the SM [68]), were considered in

TABLE II. Summary of the cohesive energies of  $\text{MB}_2\text{C}_2$  films.

Compound	$E_c$	$E'_c$
$\text{MoS}_2$ [87]	-5.07	
Graphene [88]	-9.26	
$\text{LiB}_2\text{C}_2$	-6.70	-0.86
$\text{NaB}_2\text{C}_2$	-6.32	-0.48
$\text{KB}_2\text{C}_2$	-6.06	-0.23
$\text{BeB}_2\text{C}_2$	-6.99	-1.16
$\text{MgB}_2\text{C}_2$	-6.61	-0.78
$\text{CaB}_2\text{C}_2$	-6.50	-0.66
$\text{SrB}_2\text{C}_2$	-6.18	-0.35
$\text{ScB}_2\text{C}_2$	-7.43	-1.59
$\text{YB}_2\text{C}_2$	-7.12	-1.29
$\text{LaB}_2\text{C}_2$	-7.01	-1.17
$\text{TiB}_2\text{C}_2$	-7.98	-2.15
$\text{ZrB}_2\text{C}_2$	-7.97	-2.13
$\text{HfB}_2\text{C}_2$	-8.27	-2.44
$\text{VB}_2\text{C}_2$	-8.12	-2.29
$\text{NbB}_2\text{C}_2$	-8.35	-2.52
$\text{TaB}_2\text{C}_2$	-8.34	-2.51
$\text{MoB}_2\text{C}_2$	-8.36	-2.53
$\text{WB}_2\text{C}_2$	-8.39	-2.55
$\text{MnB}_2\text{C}_2$	-7.12	-1.29
$\text{FeB}_2\text{C}_2$	-7.28	-1.45
$\text{RuB}_2\text{C}_2$	-7.50	-1.67
$\text{CoB}_2\text{C}_2$	-7.27	-1.44
$\text{AlB}_2\text{C}_2$	-6.88	-1.04

the  $M$ -B-C ternary system. These compositions were selected because they can be derived from the parent  $M$ -B-C materials. Through database and literature research on the parent materials, we found that the parent Li-B-C [86] and Ca-B-C [43] systems have complete ternary phase diagrams. Consequently, we selected thermodynamically stable bulk materials to exfoliate Li-B-C and Ca-B-C films, using them as structural prototypes to obtain other  $M$ -B-C films by replacing the metal atoms. The ternary phase diagrams of 2D  $M$ -B-C systems were constructed based on the formation energy calculations, considering the isolated atoms, binary honeycomb BC, and experimentally synthesized  $\text{BC}_3$  monolayers, as well as the proposed ternary 2D compounds. It is essential to emphasize that the artificially constructed 2D  $M$ -B-C structures do not necessarily represent global minima on the potential surface, and the seven compositions under consideration represent a limited subset; regions capable of accommodating stable phases within the convex hull may exist.

As shown in Fig. 6 and in Fig. S27 in the SM [68],  $\text{LiB}_2\text{C}_2$ ,  $\text{NaB}_2\text{C}_2$ ,  $\text{CaB}_2\text{C}_2$ , and  $\text{LaB}_2\text{C}_2$  films exhibit thermodynamic stability, as they lie on the convex hull, suggesting the potential for experimental synthesis. In contrast,  $\text{KB}_2\text{C}_2$  and  $\text{SrB}_2\text{C}_2$  films are metastable, as they are situated above the convex hull, with positive formation energies of  $\sim 62$  and  $99$  meV/atom, respectively. Despite this,  $\text{KB}_2\text{C}_2$  and  $\text{SrB}_2\text{C}_2$  films could still be synthesized experimentally, as they possess negative cohesive energies of  $-6.06$  and  $-6.18$  eV/atom (Table II), respectively. These cohesive energies are comparable to those of  $\text{MoS}_2$  [87] and graphene [88], suggesting their potential for synthesis. In addition, calculation results show that  $\text{KB}_2\text{C}_2$  and  $\text{SrB}_2\text{C}_2$  can be synthesized on the

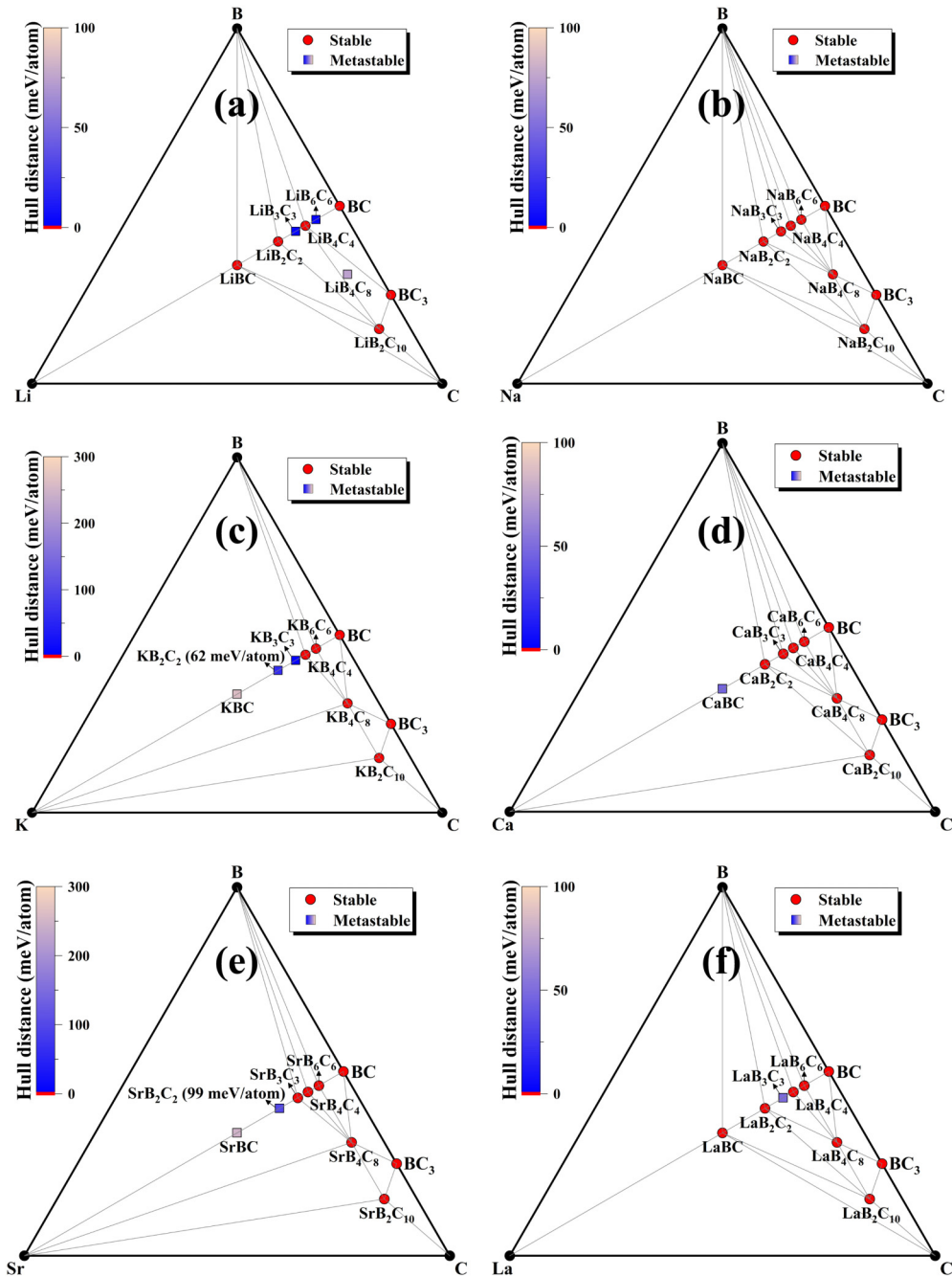


FIG. 6. The convex hull of the ternary (a) Li-B-C, (b) Na-B-C, (c) K-B-C, (d) Ca-B-C, (e) Sr-B-C, and (f) La-B-C systems.

Ag(111) surface using the molecular beam epitaxy technique, as discussed in Appendix B. Furthermore, we also identified a series of other stable metal borocarbides that could potentially exhibit superconductivity. The two descriptors proposed by us could be applied to predict the superconducting properties of the wider range of stable metal borocarbide compounds identified, beyond just the 2D  $MB_2C_2$  family.

#### APPENDIX B: POTENTIAL EXPERIMENTAL FEASIBILITY OF $MB_2C_2$ FILMS

The cohesive energies are calculated according to the following equations:  $E_c(MB_2C_2) = [E(MB_2C_2) - E_M - 2E_B -$

$2E_C]/N$  and  $E'_c(MB_2C_2) = [E(MB_2C_2) - E_M - 2E_{BC}]/N$ , where  $E(MB_2C_2)$  is the total energy of the  $MB_2C_2$  films;  $E_M$ ,  $E_B$ , and  $E_C$  are the energies of the isolated metal and B and C atoms, respectively; and  $E_{BC}$  is the energy of the hexagonal BC monolayer.  $N$  represents the number of atoms in the unit cell. Table II demonstrates that all considered  $MB_2C_2$  films exhibit the negative cohesive energies. The calculated cohesive energies relative to isolated atoms are comparable to those of MoS<sub>2</sub> [87] and graphene [88]. This suggests the potential for experimental synthesis of these 2D  $MB_2C_2$  materials.

We propose two available approaches to obtain  $MB_2C_2$  films, as indicated below. Given that bulk LiBC was already



synthesized experimentally [89], we can use high-temperature lithium deintercalation to remove Li from the bulk material, a method commonly used to synthesize  $\text{Li}_x\text{BC}$  ( $x < 1$ ) [90–93]. Another metal can then be intercalated into the delithiated phase, restoring the ordered layered morphology by suppressing defects in the BC honeycomb layers while maintaining hole doping. Commonly available mechanical cleavage or liquid exfoliation can be used to fabricate  $\text{MB}_2\text{C}_2$  films.

The molecular beam epitaxy method is a highly controlled deposition technique that allows for the precise growth of

thin films. We take the  $\text{KB}_2\text{C}_2$  film as an example. Considering the small lattice mismatch of  $\sim 4\%$  between the  $\text{KB}_2\text{C}_2$  film and the Ag(111) surface, we use Ag(111) as a suitable substrate for the growth of  $\text{KB}_2\text{C}_2$  films. The calculated binding energy of  $\text{KB}_2\text{C}_2/\text{Ag}(111)$  is  $\sim 78 \text{ meV}/\text{\AA}^2$ , higher than those ( $\sim 30\text{--}50 \text{ meV}/\text{\AA}^2$ ) of experimentally synthesized  $\beta_{12}$  borophene/Ag(111) and  $\chi_3$  borophene/Ag(111) [94], indicating the possibility of growing  $\text{MB}_2\text{C}_2$  films on the Ag(111) surface using the molecular beam epitaxy technique.

- 
- [1] L. Boeri *et al.*, *J. Phys.: Condens. Matter* **34**, 183002 (2022).
- [2] Y. Sun and M. Miao, *Chem* **9**, 443 (2023).
- [3] Y. Li, J. Hao, H. Liu, Y. Li, and Y. Ma, *J. Chem. Phys.* **140**, 174712 (2014).
- [4] D. Duan, Y. Liu, F. Tian, D. Li, X. Huang, Z. Zhao, H. Yu, B. Liu, W. Tian, and T. Cui, *Sci. Rep.* **4**, 6968 (2014).
- [5] A. Drozdov, M. Eremets, I. Troyan, V. Ksenofontov, and S. I. Shylin, *Nature (London)* **525**, 73 (2015).
- [6] H. Wang, J. S. Tse, K. Tanaka, T. Iitaka, and Y. Ma, *Proc. Natl. Acad. Sci. USA* **109**, 6463 (2012).
- [7] L. Ma *et al.*, *Phys. Rev. Lett.* **128**, 167001 (2022).
- [8] Z. Li *et al.*, *Nat. Commun.* **13**, 2863 (2022).
- [9] F. Peng, Y. Sun, C. J. Pickard, R. J. Needs, Q. Wu, and Y. Ma, *Phys. Rev. Lett.* **119**, 107001 (2017).
- [10] H. Liu, I. I. Naumov, R. Hoffmann, N. Ashcroft, and R. J. Hemley, *Proc. Natl. Acad. Sci. USA* **114**, 6990 (2017).
- [11] M. Somayazulu, M. Ahart, A. K. Mishra, Z. M. Geballe, M. Baldini, Y. Meng, V. V. Struzhkin, and R. J. Hemley, *Phys. Rev. Lett.* **122**, 027001 (2019).
- [12] A. Drozdov *et al.*, *Nature (London)* **569**, 528 (2019).
- [13] I. Errea *et al.*, *Nature (London)* **578**, 66 (2020).
- [14] Y. Li, J. Hao, H. Liu, J. S. Tse, Y. Wang, and Y. Ma, *Sci. Rep.* **5**, 9948 (2015).
- [15] I. A. Troyan *et al.*, *Adv. Mater.* **33**, 2006832 (2021).
- [16] P. Kong *et al.*, *Nat. Commun.* **12**, 5075 (2021).
- [17] E. Snider, N. Dasenbrock-Gammon, R. McBride, X. Wang, N. Meyers, K. V. Lawler, E. Zurek, A. Salamat, and R. P. Dias, *Phys. Rev. Lett.* **126**, 117003 (2021).
- [18] Y. Wang, K. Wang, Y. Sun, L. Ma, Y. Wang, B. Zou, G. Liu, M. Zhou, and H. Wang, *Chin. Phys. B* **31**, 106201 (2022).
- [19] Y. Sun, J. Lv, Y. Xie, H. Liu, and Y. Ma, *Phys. Rev. Lett.* **123**, 097001 (2019).
- [20] Y. Song, J. Bi, Y. Nakamoto, K. Shimizu, H. Liu, B. Zou, G. Liu, H. Wang, and Y. Ma, *Phys. Rev. Lett.* **130**, 266001 (2023).
- [21] J. Nagamatsu, N. Nakagawa, T. Muranaka, Y. Zenitani, and J. Akimitsu, *Nature (London)* **410**, 63 (2001).
- [22] H. J. Choi, D. Roundy, H. Sun, M. L. Cohen, and S. G. Louie, *Nature (London)* **418**, 758 (2002).
- [23] A. Bhaumik, R. Sachan, S. Gupta, and J. Narayan, *ACS Nano* **11**, 11915 (2017).
- [24] A. Bhaumik, R. Sachan, and J. Narayan, *ACS Nano* **11**, 5351 (2017).
- [25] L. Zhu *et al.*, *Sci. Adv.* **6**, eaay8361 (2020).
- [26] J.-N. Wang, X.-W. Yan, and M. Gao, *Phys. Rev. B* **103**, 144515 (2021).
- [27] S. Di Cataldo, S. Qulaghasi, G. B. Bachelet, and L. Boeri, *Phys. Rev. B* **105**, 064516 (2022).
- [28] L. Zhu *et al.*, *Phys. Rev. Res.* **5**, 013012 (2023).
- [29] H. Rosner, A. Kitaigorodsky, and W. E. Pickett, *Phys. Rev. Lett.* **88**, 127001 (2002).
- [30] M. Gao, Z.-Y. Lu, and T. Xiang, *Phys. Rev. B* **91**, 045132 (2015).
- [31] E. Haque, M. A. Hossain, and C. Stampfl, *Phys. Chem. Chem. Phys.* **21**, 8767 (2019).
- [32] T.-T. Pham and D.-L. Nguyen, *Phys. Rev. B* **107**, 134502 (2023).
- [33] K.-P. Bohnen, R. Heid, and B. Renker, *Phys. Rev. Lett.* **86**, 5771 (2001).
- [34] J. K. Dewhurst, S. Sharma, C. Ambrosch-Draxl, and B. Johansson, *Phys. Rev. B* **68**, 020504(R) (2003).
- [35] R. Miao, G. Huang, and J. Yang, *Solid State Commun.* **233**, 30 (2016).
- [36] T. Bazhurov, Y. Sakai, S. Saito, and M. L. Cohen, *Phys. Rev. B* **89**, 045136 (2014).
- [37] Y. Quan and W. E. Pickett, *Phys. Rev. B* **102**, 144504 (2020).
- [38] P. Zhang, X. Li, X. Yang, H. Wang, Y. Yao, and H. Liu, *Phys. Rev. B* **105**, 094503 (2022).
- [39] N. Geng, K. P. Hilleke, L. Zhu, X. Wang, T. A. Strobel, and E. Zurek, *J. Am. Chem. Soc.* **145**, 1696 (2023).
- [40] E. Ekimov, V. Sidorov, E. Bauer, N. Mel'nik, N. Curro, J. Thompson, and S. Stishov, *Nature (London)* **428**, 542 (2004).
- [41] F. Zheng, Y. Sun, R. Wang, Y. Fang, F. Zhang, S. Wu, C.-Z. Wang, V. Antropov, and K.-M. Ho, *Phys. Rev. B* **107**, 014508 (2023).
- [42] G. P. Kafle, C. R. Tomassetti, I. I. Mazin, A. N. Kolmogorov, and E. R. Margine, *Phys. Rev. Mater.* **6**, 084801 (2022).
- [43] C. Zhang, H. Tang, C. Pan, H. Jiang, H.-J. Sun, K.-M. Ho, and C.-Z. Wang, *Phys. Rev. B* **108**, 024512 (2023).
- [44] J.-H. Liao, Y.-C. Zhao, Y.-J. Zhao, H. Xu, and X.-B. Yang, *Phys. Chem. Chem. Phys.* **19**, 29237 (2017).
- [45] J. Bekaert, A. Aperis, B. Partoens, P. M. Oppeneer, and M. V. Milošević, *Phys. Rev. B* **96**, 094510 (2017).
- [46] J. Bekaert, M. Petrov, A. Aperis, P. M. Oppeneer, and M. V. Milošević, *Phys. Rev. Lett.* **123**, 077001 (2019).
- [47] Y. Zhao, C. Lian, S. Zeng, Z. Dai, S. Meng, and J. Ni, *Phys. Rev. B* **100**, 094516 (2019).
- [48] Z. Wang, S. Zeng, Y. Zhao, X. Wang, and J. Ni, *Phys. Rev. B* **104**, 174519 (2021).
- [49] Y. Zhao, C. Lian, S. Zeng, Z. Dai, S. Meng, and J. Ni, *Phys. Rev. B* **101**, 104507 (2020).

- [50] P. Modak, A. K. Verma, and A. K. Mishra, *Phys. Rev. B* **104**, 054504 (2021).
- [51] M. Gao, X.-W. Yan, Z.-Y. Lu, and T. Xiang, *Phys. Rev. B* **101**, 094501 (2020).
- [52] L. Liu, X. Liu, P. Song, L. Zhang, X. Huang, W. Zhang, Z. Zhang, and Y. Jia, *Nano Lett.* **23**, 1924 (2023).
- [53] S. Singh, A. H. Romero, J. D. Mella, V. Ereemeev, E. Muñoz, A. N. Alexandrova, K. M. Rabe, D. Vanderbilt, and F. Muñoz, *npj Quantum Mater.* **7**, 37 (2022).
- [54] W. Kohn and L. J. Sham, *Phys. Rev.* **140**, A1133 (1965).
- [55] G. Kresse and J. Hafner, *Phys. Rev. B* **48**, 13115 (1993).
- [56] G. Kresse and J. Furthmüller, *Phys. Rev. B* **54**, 11169 (1996).
- [57] J. P. Perdew, K. Burke, and M. Ernzerhof, *Phys. Rev. Lett.* **77**, 3865 (1996).
- [58] P. E. Blöchl, *Phys. Rev. B* **50**, 17953 (1994).
- [59] H. J. Monkhorst and J. D. Pack, *Phys. Rev. B* **13**, 5188 (1976).
- [60] S. Baroni, S. De Gironcoli, A. Dal Corso, and P. Giannozzi, *Rev. Mod. Phys.* **73**, 515 (2001).
- [61] P. Giannozzi *et al.*, *J. Phys.: Condens. Matter* **21**, 395502 (2009).
- [62] G. Kresse and D. Joubert, *Phys. Rev. B* **59**, 1758 (1999).
- [63] S. Poncé, E. R. Margine, C. Verdi, and F. Giustino, *Comput. Phys. Commun.* **209**, 116 (2016).
- [64] F. Giustino, M. L. Cohen, and S. G. Louie, *Phys. Rev. B* **76**, 165108 (2007).
- [65] E. R. Margine and F. Giustino, *Phys. Rev. B* **87**, 024505 (2013).
- [66] A. A. Mostofi, J. R. Yates, Y.-S. Lee, I. Souza, D. Vanderbilt, and N. Marzari, *Comput. Phys. Commun.* **178**, 685 (2008).
- [67] P. B. Allen and R. Dynes, *Phys. Rev. B* **12**, 905 (1975).
- [68] See Supplemental Material at <http://link.aps.org/supplemental/10.1103/PhysRevB.110.064513> for the convergence tests of superconducting gaps and the EPC constant of high- $T_c$   $MB_2C_2$  films; phonon spectra of 21 dynamically stable, metallic  $MB_2C_2$  films; band structures, PDOSs, the contributions of  $\sigma$  and  $\pi$  orbitals to the Fermi surface, and superconductive properties of 17 nonmagnetic, metallic  $MB_2C_2$  films; the electronic properties of four magnetic  $MB_2C_2$  films;  $A_g$  and  $B_u$  vibrational modes of the  $KL_aB_4C_4$  film; the band structure, PDOS, and superconductive property of the  $NaScB_4C_4$  film; and the three-dimensional convex hull diagram of high- $T_c$   $MB_2C_2$  films.
- [69] S.-Y. Xie, X.-B. Li, W. Q. Tian, N.-K. Chen, X.-L. Zhang, Y. Wang, S. Zhang, and H.-B. Sun, *Phys. Rev. B* **90**, 035447 (2014).
- [70] S.-Y. Xie, X.-B. Li, W. Q. Tian, N.-K. Chen, Y. Wang, S. Zhang, and H.-B. Sun, *Phys. Chem. Chem. Phys.* **17**, 1093 (2015).
- [71] Z. Qu, F. Han, T. Yu, M. Xu, Y. Li, and G. Yang, *Phys. Rev. B* **102**, 075431 (2020).
- [72] T. Bo, P.-F. Liu, L. Yan, and B.-T. Wang, *Phys. Rev. Mater.* **4**, 114802 (2020).
- [73] L. Yan, T. Bo, P.-F. Liu, L. Zhou, J. Zhang, M.-H. Tang, Y.-G. Xiao, and B.-T. Wang, *J. Mater. Chem. C* **8**, 1704 (2020).
- [74] J. M. An and W. E. Pickett, *Phys. Rev. Lett.* **86**, 4366 (2001).
- [75] J. Klimeš, D. R. Bowler, and A. Michaelides, *Phys. Rev. B* **83**, 195131 (2011).
- [76] F. S. Khan and P. B. Allen, *Phys. Rev. B* **29**, 3341 (1984).
- [77] P. Szabó, P. Samuely, J. Kačmarčík, T. Klein, J. Marcus, D. Fruchart, S. Miraglia, C. Marcenat, and A. G. M. Jansen, *Phys. Rev. Lett.* **87**, 137005 (2001).
- [78] R. S. Gonnelli, D. Daghero, G. A. Ummarino, V. A. Stepanov, J. Jun, S. M. Kazakov, and J. Karpinski, *Phys. Rev. Lett.* **89**, 247004 (2002).
- [79] M. Iavarone *et al.*, *Phys. Rev. Lett.* **89**, 187002 (2002).
- [80] Y. Sun, F. Zhang, C.-Z. Wang, K.-M. Ho, I. I. Mazin, and V. Antropov, *Phys. Rev. Mater.* **6**, 074801 (2022).
- [81] Y. Wang, J. Lv, L. Zhu, and Y. Ma, *Phys. Rev. B* **82**, 094116 (2010).
- [82] Y. Wang, J. Lv, L. Zhu, and Y. Ma, *Comput. Phys. Commun.* **183**, 2063 (2012).
- [83] Y. Wang, M. Miao, J. Lv, L. Zhu, K. Yin, H. Liu, and Y. Ma, *J. Chem. Phys.* **137**, 224108 (2012).
- [84] B. Gao, P. Gao, S. Lu, J. Lv, Y. Wang, and Y. Ma, *Sci. Bull.* **64**, 301 (2019).
- [85] X. Shao, J. Lv, P. Liu, S. Shao, P. Gao, H. Liu, Y. Wang, and Y. Ma, *J. Chem. Phys.* **156**, 014105 (2022).
- [86] S. Kharabazde, M. Meyers, C. R. Tomassetti, E. R. Margine, I. I. Mazin, and A. N. Kolmogorov, *Phys. Chem. Chem. Phys.* **25**, 7344 (2023).
- [87] Y. Ding, Y. Wang, J. Ni, L. Shi, S. Shi, and W. Tang, *Phys. B (Amsterdam, Neth.)* **406**, 2254 (2011).
- [88] R. Majidi, *Theor. Chem. Acc.* **136**, 109 (2017).
- [89] A. Bharathi, S. J. Balaselvi, M. Premila, T. Sairam, G. Reddy, C. Sundar, and Y. Hariharan, *Solid State Commun.* **124**, 423 (2002).
- [90] L. Zhao, P. Klavins, and K. Liu, *J. Appl. Phys.* **93**, 8653 (2003).
- [91] A. Fogg, J. Claridge, G. Darling, and M. Rosseinsky, *Chem. Commun.* **93**, 1348 (2003).
- [92] A. M. Fogg, J. Meldrum, G. R. Darling, J. B. Claridge, and M. J. Rosseinsky, *J. Am. Chem. Soc.* **128**, 10043 (2006).
- [93] B. Kalkan and E. Ozdas, *ACS Appl. Mater. Interfaces* **11**, 4111 (2019).
- [94] B. Feng, J. Zhang, Q. Zhong, W. Li, S. Li, H. Li, P. Cheng, S. Meng, L. Chen, and K. Wu, *Nat. Chem.* **8**, 563 (2016).